The Planetary Science Journal, 4:145 (13pp), 2023 August https://doi.org/10.3847/PSJ/ace88d

OSSOS. XXIX. The Population and Perihelion Distribution of the Detached Kuiper Belt

Matthew Beaudoin[1], Brett Gladman[1], Yukun Huang (黄宇坤)[1], Michele Bannister[2], J. J. Kavelaars[3], Jean-Marc Petit[4], and Kathryn Volk[5]
[1] Department of Physics & Astronomy, University of British Columbia, 6224 Agricultural Road, Vancouver, BC V6T 1Z1, Canada
[2] School of Physical and Chemical Sciences—Te Kura Matū University of Canterbury, Private Bag 4800, Christchurch 8140, New Zealand
[3] Herzberg Astronomy and Astrophysics Research Centre, National Research Council, 5071 West Saanich Road, Victoria, BC V9E 2E7, Canada
[4] Institut UTINAM UMR6213, CNRS, Université Bourgogne Franche-Comté, OSU Theta F-25000 Besaçon, France
[5] Lunar and Planetary Laboratory, The University of Arizona, 1629 East University Boulevard, Tucson, AZ 85721, USA
Received 2022 August 5; revised 2023 June 3; accepted 2023 June 19; published 2023 August 21

Abstract

The detached trans-Neptunian objects (TNOs) are those with semimajor axes beyond the 2:1 resonance with Neptune that are neither resonant nor scattering. Using the detached sample from the Outer Solar System Origins Survey (OSSOS) telescopic survey, we produce the first studies of their orbital distribution based on matching the orbits and numbers of the known TNOs after accounting for survey biases. We show that the detached TNO perihelion (q) distribution cannot be uniform but is instead better matched by two uniform components with a break near $q \approx 40$ au. We produce parametric two-component models that are not rejectable by the OSSOS data set and estimate that there are $36{,}000^{+12{,}000}_{-9000}$ detached TNOs with absolute magnitudes $H_r < 8.66$ ($D \gtrsim 100$ km) and semimajor axes 48 au $< a < 250$ au (95% confidence limits). Although we believe that these heuristic two-parameter models yield a correct population estimate, we then use the same methods to show that the perihelion distribution of a detached disk created by a simulated rogue planet matches the q distribution even better, suggesting that the temporary presence of other planets in the early solar system is a promising model to create today's large semimajor axis TNO population. This cosmogonic simulation results in a detached TNO population estimate of $48{,}000^{+15{,}000}_{-12{,}000}$. Because this illustrates how difficult-to-detect $q > 50$ au objects are likely present, we conclude that there are $(5 \pm 2) \times 10^4$ dynamically detached TNOs, roughly twice as many as in the entire trans-Neptunian hot main belt.

Unified Astronomy Thesaurus concepts: Detached objects (376); Trans-Neptunian objects (1705); Small Solar System bodies (1469); Kuiper belt (893)

1. Introduction

Trans-Neptunian objects (TNOs) are considered to be leftovers from the early stages of planet formation in the solar system, when the Sun was still surrounded by a protoplanetary disk. By the time the four giant planets had formed and the young Sun's solar wind had expelled the gas and remaining dust, planetesimals existed all across the outer solar system. At the very least, this included millions of objects with diameters of $D > 50$ km, all the way up to a set of dwarf planet–sized objects (reaching a few thousand kilometers across, such as Pluto), and then a uniform number of planetary objects.

The most-discussed paradigm is that the TNO region beyond Neptune consists of two components. The "cold classical Kuiper Belt" has various historical definitions but has recently been commonly restricted to the main belt's low-inclination component, which seems to exist only on low-eccentricity orbits from semimajor axes of $a = 42.4$ to 47.5 au. This current cold belt has been suggested (Kavelaars et al. 2021) to be a largely unaltered remnant preserving the original formation size distribution and cold TNO number (of approximately 10^4 objects with $D > 100$ km). In contrast, the more numerous "hot" population (hot in terms of orbital eccentricity e and inclination i) is generally thought to have formed closer to the Sun and then scattered out with some small fraction decoupled from Neptune's influence and preserved to the present day (see reviews by Morbidelli et al. 2008; Nesvorný 2018; Gladman & Volk 2021). In this scenario, all of the hot populations from Neptune Trojans (co-orbitals librating around Lagrange points) to the Oort cloud share a common origin. Petit et al. (2011) showed that the number density of objects from 30 to 100 au across the inner belt (closer to Neptune than the 3:2 resonance), the main belt (from the 3:2 to 2:1), and the region beyond the 2:1 at 48 au could be smoothly connected. Beyond 48 au, there is either no cold belt or a sudden dramatic drop in the surface density (Gladman & Volk 2021); the stable TNOs consist of only those hot-population objects trapped in distant mean-motion resonances (MMRs) and the "detached" population. After initial scattering to large a, the detached objects had their perihelia distance q raised by unclear processes to values beyond which Neptune can strongly influence them today.

In this paper, we define "detached" objects as the TNOs beyond the Neptune 2:1 MMR ($a > 48$ au) that are neither (mean-motion) resonant nor scattering per the classifications described in Gladman et al. (2008). Scattering objects have semimajor axes that can be significantly altered by gravitational interactions with Neptune on Myr timescales (see Gladman et al. 2008). Roughly speaking, detached TNOs have large enough perihelia to be dynamically decoupled from Neptune, thus avoiding significant gravitational interaction (scattering) on 10 Myr to Gyr timescales; the amount of mobility and the scattering timescale depend on a and q (see Gladman et al. 2002; Bannister et al. 2017; Khain et al. 2020; Batygin et al. 2021). Other dynamical classes of TNOs have origins and

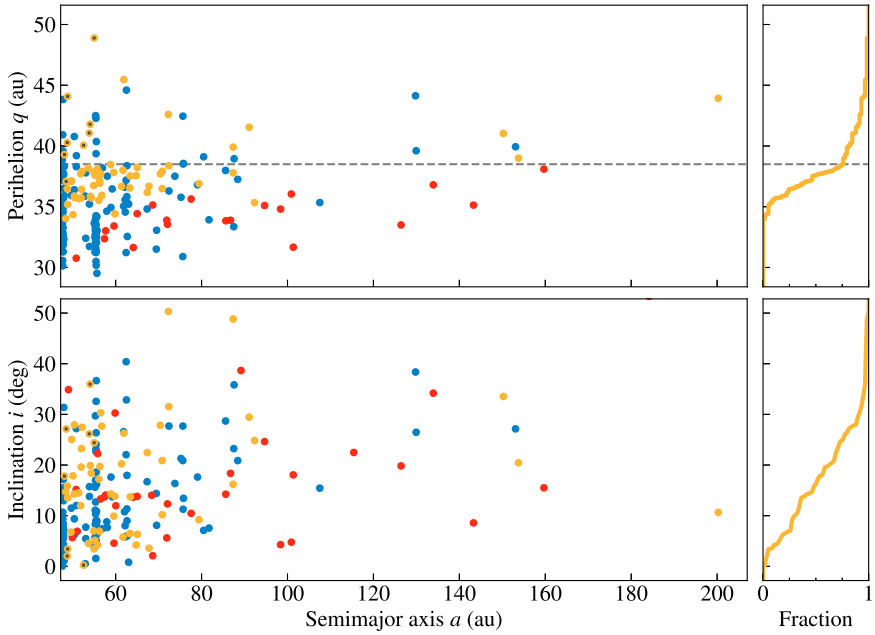

Figure 1. Detached (gold points) TNO sample from OSSOS. The $q = 38.5$ au horizontal dashed line in the upper a, q plot highlights a break in the cumulative perihelion distribution (upper right plot). The eight OSSOS "outer classicals" we adopt as detached (see text) are indicated by overlaid black squares. Scattering objects (red) and objects in MMRs (blue) are diagnosed via 10 Myr numerical integration and plotted for reference. Three obvious resonant semimajor axes are 48 (2:1), 55 (5:2), and 63 (3:1) au; the resonances stabilize even $q < 34$ au TNOs. Note that there are strong detection biases against objects in the upper right of each of the two distributions. The cumulative distributions (right panels) are only for the detached sample. The inclination distribution (bottom) is not obviously different among the three populations, although the 2:1 resonance is relatively poor in large-i TNOs (Chen et al. 2019).

emplacement mechanisms that are mostly understood and only require the action of the known planets (Duncan & Levison 1997; Morbidelli et al. 2008; Malhotra 2019). The physics of perihelion lifting for detached TNOs are unclear, but there are many ideas, including dynamical diffusion (Bannister et al. 2018), dropouts from MMRs during grainy Neptune migration (Kaib & Sheppard 2016; Nesvorný et al. 2016) and/or Neptune's orbital circularization phase (Pike & Lawler 2017), interactions with a distant giant planet (Gomes et al. 2006; Lawler et al. 2017), a stellar flyby (Morbidelli & Levison 2004), perturbations in the solar birth cluster (Brasser & Schwamb 2015), and the action of a rogue planet that was scattered to the outer solar system and lifted the perihelia before being ejected (Gladman et al. 2002; Gladman & Chan 2006; Silsbee & Tremaine 2018).

In the way this paper (and past papers from the Canada–France Ecliptic Plane Survey, CFEPS/Outer Solar System Origins Survey, OSSOS, collaboration that estimate populations) approaches the problem, if one is going to compare a cosmogonic numerical simulation to observations, then one determines the 10 Myr behavior of the simulation's orbits at the current epoch and divides them exactly the same way as the dynamical classification of observed objects. That is, one determines which of the simulation's particles are resonant and which are scattering on a 10 Myr interval, and the remainder are detached. Thus, when we provide a measure of a "detached population," we are providing the population of nonresonant TNOs beyond the 2:1 that are not scattering on 10 Myr timescales.

There is only one observational estimate of the number of dynamically detached objects in the literature. As one result of the CFEPS, Petit et al. (2011) estimated the number of detached objects with $a > 48$ au to be $N(H_g \leqslant 8) = 10{,}000^{+7000}_{-5000}$, with the uncertainties representing a 95% confidence interval. It is important to note that Petit et al. (2011) used a very small sample of only 13 detached objects. Due to this paucity of objects, they adopted the same q and i distributions as for the hot main belt, which are purely empirical models based on the observed distribution of hot main-belt classical TNOs. Thus, there is currently no population estimate of the detached objects with independently determined orbital element distributions. Based on the nonrejectable parametric models we describe in this paper, we produce such an estimate. Population estimates serve as a goalpost for emplacement models, in the sense that any model must reproduce the intrinsic population to be considered valid. The relative population of associated dynamical classes is also of interest for physical models; for example, what is the ratio between the detached and resonant populations in the $a = 48$–250 au range?

In this paper, we make use of the TNO catalog from the OSSOS++ collections of characterized surveys, comprised of OSSOS (Bannister et al. 2016, 2018), CFEPS (Petit et al. 2011), the CFEPS High-latitude Component (Petit et al. 2017), and the Alexandersen et al. (2016) survey. With a vastly increased sample of detections resulting from the OSSOS++ suite, we can now quantitatively explore the orbital element and size distributions of the detached objects from their inner boundary at the Neptune 2:1 MMR ($a \simeq 48$ au) to $a = 250$ au. The OSSOS collection provides 58 objects that numerically demonstrate detached behavior (nonresonant and nonscattering on 10 Myr timescales) having perihelia of $q = 34.03$–48.89 au; no $q < 34$ au OSSOS object demonstrates detached behavior. For the purposes of this paper, we include in our set of $a > 48$ au detached objects eight "outer classicals" (see Figure 1) having $a = 48$–55 au with eccentricity $e < 0.24$ (see Bannister et al. 2018). According to the Gladman et al. (2008) classification scheme, nonscattering and nonresonant objects beyond the 2:1 are nominally detached only if they have

$e > 0.24$; for this work, we are adopting the viewpoint that these eight OSSOS outer classicals were emplaced by the same mechanisms as the other detached TNOs, so we include them in our list. Motivated by the largest-a object in the OSSOS++ detached sample, 2013 UT_{15} (OSSOS designation o3l83) with $a \simeq 200$ au, and the relative sparsity of larger-a objects, we will thus only give the orbital element, H magnitude, and population constraints for objects with $a < 250$ au. Beyond this, there are very few objects, especially at large q, which were found in a large variety of different solar system surveys that we are unable to rigorously debias. This includes the realm of the so-called "extreme TNOs" (with only vaguely defined motivations for the inner a boundary); that population is in addition to what we measure in this manuscript and could include a significant population of $q \gg 50$ au TNOs (like Sedna and 2012 VP113, with $q \simeq 75$ and 80 au, respectively) but with $a > 250$ au.

Figure 1 shows the (a, q) and (a, i) distributions of TNOs in this semimajor axis range. Histograms on the right of each panel show the cumulative distributions in q and i; one obvious feature in the q distribution of the detached objects is the apparent rollover at $q \simeq 38.5$ au. Can this feature be explained by observational bias and preferential detection of low-q objects? Or is it real and some kind of indicator for the perihelion-lifting mechanism? To answer these questions, we use the OSSOS Survey Simulator (Petit et al. 2011, 2018), which applies the observational bias from which the real TNO detections suffer to a given model (Lawler et al. 2018a). By comparing the simulated detections to the real objects, we are thus able to evaluate the suitability of various models for the detached objects' intrinsic q distribution with a focus on the aforementioned rollover.

We first explore empirical models that are nonrejectable matches to the distribution of observed detached TNOs, providing an estimate of the intrinsic detached population. We then briefly study an example of matching a cosmogonic numerical simulation of the orbital distribution that results from the hypothetical presence of an additional rogue planet (one formed in the solar system that is eventually ejected via gravitational scattering), showing that the resulting observationally biased perihelion distribution from that simulation bears a striking resemblance to the known detections.

2. Survey Simulations of Orbit and Size Distributions

The concept of a survey simulator is straightforward; given intrinsic distributions of orbital elements, the software creates an object by randomly drawing from them, places it on the sky, applies all of the observational biases of a characterized survey, and reports if the object would have been detected (for in-depth discussions, see Kavelaars et al. 2009; Lawler et al. 2018a). Providing the survey simulator with parametric distributions allows the model to be attenuated by the observational biases. To do this, a synthetic object that is randomly drawn from the intrinsic distribution is exposed to the biases of the survey, including field of view (it must be within the survey's coverage), CCD filling factor, rate cuts, tracking fraction (near unity for OSSOS, the largest survey in our ensemble), and detection efficiency. For example, a TNO may be drawn at a sky position that happens to be in a field of the survey, but its magnitude may be too faint for detection. The most important criterion for detection, after the on-sky location, is the object's magnitude; whether or not the object is detected in a field depends heavily on the detection efficiency function of the observation block/field.

First, we provide parametric distributions of a, q, i, and H to the survey simulator, and the output is a list of properties of the objects that were drawn and those that were tracked. The collection of tracked objects comprises our "simulated detections." The survey simulator is usually set to run until a large number of simulated objects are found to ensure well-sampled cumulative distribution functions (CDFs), to which we compare the small set of real detections.

Because these models include difficult-to-detect TNOs, the simulator must draw enormous numbers of randomized intrinsic objects (most of which are then not observed) to get a statistically useful number of simulated detections. In our models, millions of candidate TNOs must be examined before ~5000 tracked detections are made. This ratio is indicative of how much larger the true population is than the detected number.

The survey simulator can also operate in "lookup" mode (as opposed to "parametric" mode). In this case, instead of randomly drawing from distributions, it draws objects from a lookup table and exposes them to the survey biases; such lookup tables are most often the result of an orbital simulation with a physical motivation. The OSSOS Survey Simulator can run until it reaches the end of the lookup table or a specified number of simulated detections are obtained. This can lead to drawing the same model TNO multiple times; this is often dealt with by randomizing angular variables and implementing a very small "fuzzing" of orbital elements (no more than $\pm 0.5\%$) to allow for more simulated detections than a model might provide. In Section 5, we forward-bias the results of a rogue planet scenario integration using the survey simulator in lookup mode.

Following methodically similar projects in the literature (Kavelaars et al. 2009; Shankman et al. 2013, 2016; Alexandersen et al. 2016; Bannister et al. 2016; Lawler et al. 2018b), we examine the rejectability of a model using a "bootstrapped" Anderson–Darling (A-D) goodness-of-fit test (Anderson & Darling 1954), which tests the hypothesis that a sample originated from a specified population. The A-D statistic is conceptually similar to the Kolmogorov–Smirnov (K-S) statistic (which is the extremum of the difference between the two distributions). We prefer the A-D methodology for our tests, as it is more sensitive to differences at the tails of the distributions than the K-S test. In what follows, in all but one case, we use the A-D test to establish confidence intervals around the model parameters and "reject" a parameter set when the A-D probability is $p < 0.05$.

In order to estimate model rejectability, one must bootstrap the distribution of A-D statistics (e.g., Kavelaars et al. 2009; Gladman et al. 2012; Shankman et al. 2016; Lawler et al. 2018b). We run the survey simulator to generate a set of simulated detections (typically 3000–10,000) that is much larger than the number of known objects. First, the "real" A-D statistic between the observed objects and simulated detections from a model is calculated. We then randomly select a subsample from the simulated detections that is the same size as the number of real objects, computing the A-D statistic between it and the simulated distribution. By repeating this process many thousands of times, one bins them to estimate the bootstrapped A-D statistic distribution. We then look at the probability of obtaining an A-D statistic greater than the "real"

A-D statistic; if <5% of the simulated statistics are greater than the real statistic, and thus the probability is <5%, we conclude that the model distribution is inconsistent with observations and reject it at the 95% confidence level (or, similarly, <1% determines 99% confidence). We refer to this probability as the "A-D test result/probability" or just as probability P. This quantity can be thought of as an "acceptability criterion," or $1-P$ as the rejection confidence.

The above process applies to each parameter of interest (a, q, H, and i); here we treat each parameter as independently rejectable. It is possible to run a multiparameter A-D model rejection test (e.g., Alexandersen et al. 2016; Lawler et al. 2018a), but correlations between parameters (especially a, q, and H) make it difficult to find specific areas of issue that cause the entire model group to be rejected. This is more applicable to parametric models, where each distribution is tweaked to fit a known population. When forward-biasing the results of a numerical integration, it can be useful to have a total rejection criterion. However, we maintain single-parameter A-D testing throughout to attempt to identify specific discrepancies in particular orbital elements.

When considering implantation into the Kuiper Belt, we find that the q distribution is the critical element, as it measures how much perturbation is needed to convert a Neptune-coupled orbit to one that is detached (since TNOs are scattered to a very large e range but a much more limited q range). Thus, the a and e distributions are largely set by basic Neptune scattering, while the q distribution is much more sensitive to the detachment physics. The e distribution of the scattering and detached TNOs is so broad that it mutes the signature of the critical perihelion distribution, and because the q range is much narrower than the a and e ranges, the latter two quantities are very correlated, so testing each provides nearly the same statistical information. For this reason, we examine the q distribution instead of the e distribution and find that this choice allows for tighter constraints on nonrejectable orbital element distributions.

Since the overall goal of the survey simulator is to compare model orbital and size distributions of the outer solar system to distributions as observed by a survey, we must develop intrinsic distributions to test. We will test a number of potential detached object distributions for both size (H magnitude) and orbital elements guided by previous studies (Shankman et al. 2013, 2016; Lawler et al. 2018b). We first find i, a, and H distributions for the detached objects that are nonrejectable, basing them on models describing other TNO populations. Since we do not know the dynamics behind the detached objects' perihelion lifting, there is no expectation for the shape of the intrinsic q distribution. We gradually increase the complexity of models from the simplest case, a uniform q distribution, looking for models that we cannot reject by the statistical method described above. Then, in Section 4.1, we use a nonrejectable parametric model to estimate the population of the detached objects.

2.1. Inclination Distributions

The main-belt TNO inclination distribution is well described by $\sin(i)$ multiplied by overlapping Gaussians (Brown 2001). Individual populations outside the main belt are often fit by $\sin(i)$ times a single Gaussian,[6] with a width σ_i (e.g., Petit et al. 2011, 2017; Gladman et al. 2012; Bannister et al. 2018), of the form

$$P(i) \propto \sin(i)\exp\left(\frac{-i^2}{2\sigma_i^2}\right).$$

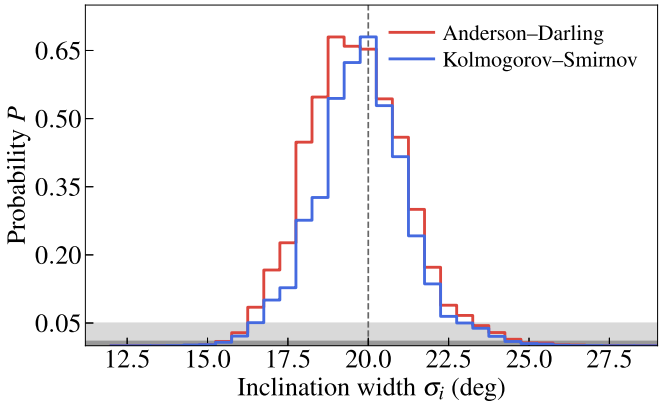

Figure 2. Bootstrapped probability of the width σ_i of an intrinsic detached TNO inclination distribution of the form $\sin i \times \exp[-i^2/(2\sigma_i^2)]$. Light and dark gray horizontal bands at the bottom denote rejection at 95% and 99% confidence intervals, respectively. Both the K-S and A-D tests for inclination agree that a model with a width $\sigma_i \simeq 20°$ is a good representation of the intrinsic distribution and reproduces the OSSOS detections. The tests shown were performed with the least-rejectable two-component q distribution as described in Section 4.

In our parametric models, we find that permitted values of the i distribution width are largely independent of the assumed a and q distributions. Testing models with very different σ_i only modifies the A-D test result of the a and q distributions by a few percent at most compared to the least-rejectable σ_i, and in no case does it shift an acceptable result to a rejectable one. With this established, we want to determine a nominal σ_i to use in our models and treat it as a fixed value when investigating the q distribution. To do so, we run the survey simulator for $\sigma_i = 12°$–$31.^\circ5$ with a step size of $0.^\circ5$. For each iteration, we generate 10,000 simulated detections and compute the A-D test result. In Figure 2, the y-axis is the probability P that a bootstrapped A-D statistic for a model with width σ_i is greater than the real A-D statistic. We reject models with $P < 5\%$ and 1% with 95% and 99% confidence, respectively. We find a least-rejectable inclination width of $\sigma_i = (20 \pm 3)°$, where the uncertainties cover the 95% confidence interval.

For comparison, the hot classical i distribution can be described by the same function with $\sigma_i = 14.^\circ5$ (Petit et al. 2017). Likewise, scattering TNOs have been modeled with an initial $\sigma_i = 12°$, which is then dynamically eroded, increasing the width by a few degrees (Shankman et al. 2013, 2016). Our result of $\sigma_i = 20°$ suggests a somewhat hotter inclination distribution for detached objects than for the hot main-belt and scattering TNOs but is comparable to distant TNOs in large-a resonances (Crompvoets et al. 2022). In particular, a wider i distribution than the hot classicals implies that the detached objects become more dispersed in inclination than the population that was initially scattered out. That is, the q-raising process that detaches TNOs likely simultaneously raises their inclinations (e.g., Gomes et al. 2008).

2.2. Semimajor Axis and Absolute Magnitude Distributions

For the models in this paper, the semimajor axis is differentially distributed according to a power law proportional

[6] Functional forms other than Gaussians are described by Gulbis et al. (2010).

to $a^{-\beta}$, where we take $\beta = 2.5$. This index for the a distribution is characteristic of an early scattering disk (Huang et al. 2022). As further motivation for this choice, Petit et al. (2011) found that a single continuous primordial hot population distributed according to the $a^{-2.5}$ power law can account for the inner belt, the hot main belt, and the detached TNOs.

The lower-a limit for our study is based on our definition of detached objects. For that population, the lower limit on a can be taken to be the outer edge of the 2:1 MMR at $a_{\min} = 48$ au (Gladman et al. 2008). Based on the largest-a detached TNO in the sample and to ensure that the large-a tail of the simulated detections is statistically robust, we adopted an upper a limit of $a_{\max} = 250$ au. There are only a few (three to five) detached objects with $a > 250$ au, and much further than that, passing stars and galactic tides are nontrivial at the object's aphelion (Sheppard et al. 2019), which may alter the power law. If the hypotheses that a massive planet still exists in the outer solar system are true (Trujillo & Sheppard 2014; Batygin et al. 2019), the semimajor axis distribution will be modified (Lawler et al. 2017). Given our interest in the apparent perihelion break around $q \simeq 38.5$ au (which is only sampled by OSSOS at low a), the 250 au upper limit on a is appropriate. Due to no OSSOS detections, our study is insensitive to the orbital distribution beyond that in any case.

We found that this semimajor axis distribution is rarely rejectable for any of our chosen H, i, and q distributions. This may be surprising because it implies that the early scattered disk (from which the detached objects are being lifted) may not have reached the expected long-term steady state of $dn/da \propto a^{-1.5}$. We will return to this topic in Section 6.

The absolute magnitude (H) distribution is motivated by studies of other TNO populations. Throughout this paper, H magnitudes are reported in the r band. In general, simple H distributions often take the form of a base-10 exponential law with a CDF of the form $N(<H) \propto 10^{\alpha H}$, where $N(<H)$ is the number of objects with absolute magnitude less than H, and α is the "slope," referring to the distribution's appearance on a logarithmic scale.[7] It is common that a single-slope H distribution is inadequate for describing a TNO population. Models with different slopes over different H ranges include broken or rolling power laws that transition to shallow slopes at large $H > 8.5$ (e.g., Bernstein et al. 2004; Fraser et al. 2014; Lawler et al. 2018b). However, at the bright end, it has long been apparent (e.g., Brown 2008) that the dwarf planets are overabundant at $H < 3$, so the "break" is in the opposite sense. Here we adopt a broken power law with two independent slopes: a shallow α_{dp} for the bright (dwarf planet) end of the distribution and a steeper α_* for $H > 3$, separated by some transition magnitude $H_{\rm break}$. Ashton et al. (2021) found that all known large TNOs could be represented by a two-component exponential law with $\alpha_{dp} = 0.14$, $\alpha_* \simeq 0.6$, with a break at $H_{\rm break} = 3$. We adopt these parameters for the detached H distribution, since there is no detached-specific distribution in the literature, and we have almost no sensitivity to $H > 8.5$.

Although we used a minimum value of $H = 0$, we show below that OSSOS is insensitive to the detached dwarf planet regime,[8] since not enough detached TNOs were detected; they make up $\ll 1\%$ of a detected sample. Since so few bright objects are drawn, it does not make a difference if the bright limit is set to $H = 0$ or down to Pluto's magnitude of $H \simeq -3$, for example. We set a faint-end H limit of $H = 9$, which is $\sim$0.5 mag fainter than the point at which one can no longer trust the survey simulator's assessment of detection efficiency. Objects drawn beyond $H = 8.5$ are, on average, at the limit of survey sensitivity, and the sharp, exponential drop-off in detection efficiency makes the survey simulator sensitive to small variations in H. The faint-end limit is set fainter than the limit we will use for our population estimate ($H_r = 8.66$), since the observed H of a simulated object can be brighter or fainter than the intrinsic H as drawn from the distribution due to the simulator modeling the photometric variation of the modeled objects.

If the object is marked as "detected," the apparent magnitude at detection is converted to a surmised absolute magnitude $H_{\rm sur}$ using the heliocentric distance. We do not know the intrinsic H magnitude for any real detached TNO. Rather, observations can only tell us the surmised magnitude. Similarly, simulated detections can appear brighter or fainter than they "really" are, and our simulated detections at the faint limit rely on the correctness of the survey simulator's low signal-to-noise ratio photometric scatter models. We found that the $\alpha_* = 0.6$ intrinsic distribution does an admirable job of representing the H magnitudes of the detected detached TNOs for our models down to the detection limit near $H \simeq 8.5$.

3. Uniform Perihelion Distribution

Recall the question of the "perihelion break" as introduced in Section 1 and illustrated in Figure 1. In the cumulative distribution, this appears as a sharp change in the slope around $q \simeq 38.5$ au. We wish to create a parametric model describing the detached object's q distribution to forward-bias using the survey simulator, testing whether this break could be entirely due to bias or if it is instead a feature in the intrinsic population.

We first test the case of a uniform distribution in perihelion, expecting to strongly reject it. One does expect the observational bias to favor low-q detections and shift the constant-slope CDF in q, but whether it can alter the distribution to the extent observed in the real objects requires survey simulation. The smallest- and largest-q detached TNOs in our sample have $q = 34.03$ and 48.89 au. To cover the full range of detached objects, we thus fix $q_{\min} = 34$ and $q_{\max} = 49$ au. The lower limit is roughly the same as the minimum q a detached object could have without scattering. In these parametric models, we are only attempting to model the perihelion distribution at a heuristic level; we primarily desire a nonrejectable model to produce a population estimate (and we show below that this population estimate is nearly independent of the details of the assumed q distribution).

Figure 3 shows the cumulative distributions of the real detached objects and the survey simulator output for the case with intrinsic q uniformly distributed between 34 and 49 au. This uses the nominal parametric models for i, a, and H as described in Sections 2.1 and 2.2. The semimajor axis and inclination distributions show the expected strong detection biases to smaller values; without a survey simulator, the magnitude of this bias is difficult to estimate. The intrinsic $a^{-2.5}$ power law and the Gaussian inclination width of $\simeq 20°$ match the OSSOS detections well, with A-D probabilities of 91% and 62%, respectively. The H_r magnitude distribution A-D probability is 57%, which is also completely acceptable, although the eye can see that $H_r < 7$ detections are slightly

[7] A cumulative diameter distribution $N(>D) \propto D^{-Q}$ corresponds to an H distribution with $\alpha = 5Q$.

[8] Eris is a prominent example.

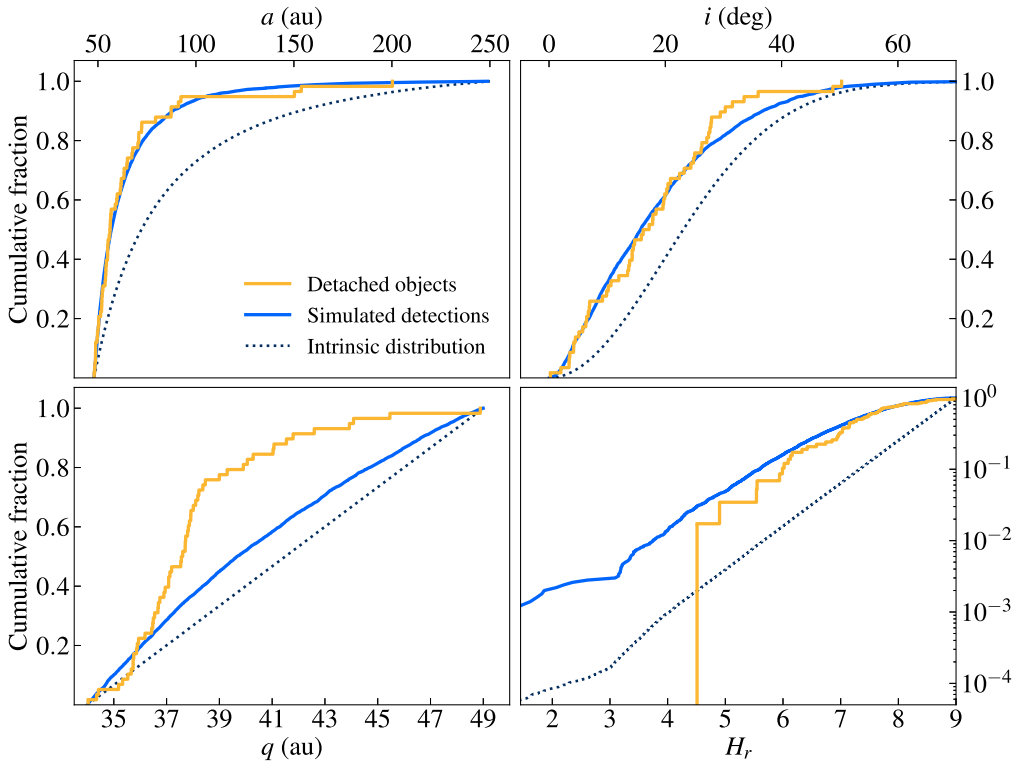

Figure 3. Cumulative distributions for a straw-man model with a uniform perihelion distribution. Each cumulative panel shows the OSSOS detached sample (gold), the intrinsic model (dotted black curves), and the simulated detection distribution from that intrinsic model after biasing by the OSSOS Survey Simulator. Although the a, q, and H_r distributions are not statistically rejectable, the lower left panel shows that despite a mild preference for detecting low-q detached objects, the detection biases cannot produce such a dramatic concentration to $q < 38.5$ au (with an A-D bootstrapped probability of drawing the observed sample from this model of <0.01%).

overproduced with this orbital and H_r magnitude distribution. The bootstrapped A-D test applied to the perihelion distribution finds, as expected, that the uniform q model can be strongly rejected at >99.99% confidence.

4. Two-component Perihelion Distribution

Evidently, the detached objects are not uniformly distributed in perihelion, even after accounting for bias. We observe only a small biasing effect in the q panel of Figure 3; there is a slight preference toward detecting objects at low q, as expected, but we do not see any indication of the sharp perihelion break that is observed in the real detached population (Figure 1).

It is clear that the data require a distribution that accounts for the abrupt change in slope around $q \simeq 38.5$ au. A simple increase in complexity is to introduce a two-component distribution that is the union of two uniform distributions; we use the label $q_{\rm split}$ as the parameter that separates each component. That is, object perihelia are distributed uniformly between $q_{\rm min}$ and $q_{\rm split}$ and between $q_{\rm split}$ and $q_{\rm max}$. The second parameter, $f_{\rm low}$, denotes the fraction of the population in the "lower" uniform distribution between $q_{\rm min}$ and $q_{\rm split}$. Note that $f_{\rm low} = 1$ corresponds to the single-component uniform case with $q_{\rm max} = q_{\rm split}$. Because the biased model must be capable of producing simulated detections with q as large as 49 au (the largest-q OSSOS detached object), we study a grid of models with a maximum value of $f_{\rm low} = 0.99$; for 10^4–10^5 simulated detections, such models provide sufficient detections in the high-q tail to properly test the rejectability of the full q range of 34–49 au.

To determine the least-rejectable ($q_{\rm split}$, $f_{\rm low}$) pair, we run a test similar to that of the inclination width but in two dimensions. Over a grid with $q_{\rm split}$ ranging from 37.5 to 43 au in 0.5 au steps and $f_{\rm low}$ ranging from 0.49 to 0.99 in steps of 0.05, we generate 10,000 simulated detections at each coordinate. We then use bootstrapped A-D statistics to evaluate the rejectability of the perihelion distribution described by each pair of parameters. The results of this test are shown by the contour plot of Figure 4. We are able to reject most combinations of ($q_{\rm split}$, $f_{\rm low}$), with a correlation between them for the nonrejectable results. We choose the least-rejectable pair as our nominal parametric perihelion distribution, which has the parameters $q_{\rm split} = 40.5$ au and $f_{\rm low} = 0.79$. Importantly, no model described on this grid has an A-D test result above 14%, which tells us in general that the "uniform" two-component q distribution is an incomplete description of the detached objects.

Using the preferred parameters described above (and the prescribed a, H, and i distributions), we now generate 5000 simulated detections to test the overall acceptability of this model. Figure 5 shows the cumulative distributions of the simulated detections and real objects for our preferred parametric model; none of the distributions for a, q, i, or H are rejectable in this case (see caption). Since we rejected the intrinsically uniform q model but are unable to reject those with slope breaks in the range of ∼38–42 au, it must be the case that the perihelion drop-off in the detached objects is a real physical phenomenon in the intrinsic population.

In the only other model used to estimate the observationally debiased number of detached objects, Petit et al. (2011) implemented a q distribution borrowed from their description

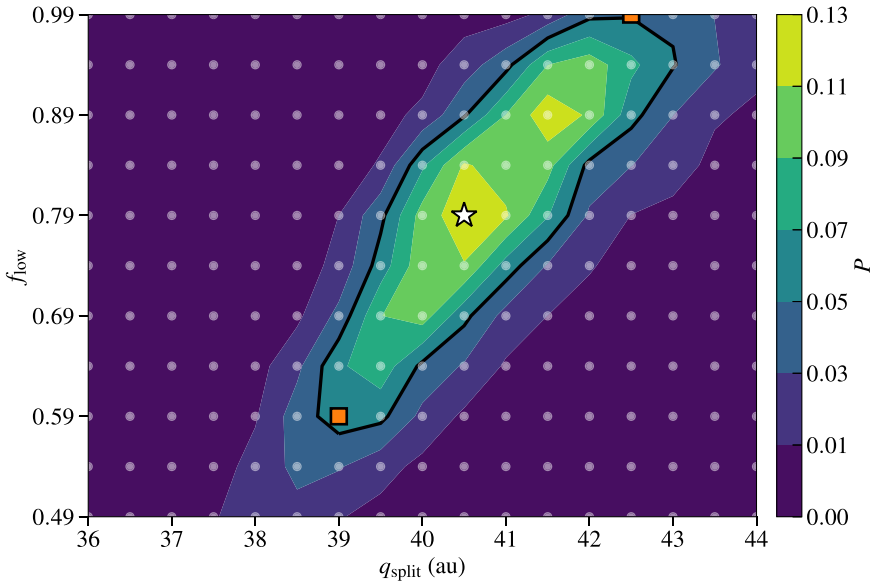

Figure 4. Contour plot of A-D probability for a grid of q_{split} and f_{low} values in the two-component perihelion model. The solid black line indicates the boundary outside of which we can reject a model at 95% confidence or higher. The star represents the (q_{split}, f_{low}) pair chosen for our least-rejectable distribution ($q_{split} = 40.5$ au, $f_{low} = 0.79$). Orange squares indicate the two "threshold" cases shown in the middle and bottom panels of Figure 6 and used for comparison population estimates in Section 4.1. A uniform distribution (strongly rejected) would have $q_{split} = 49$ au and $f_{low} = 1.0$.

of the hot main-belt classicals. It is mostly uniform between 35 and 40 au with a transition to a weak exponential tail beyond 40 au (see Appendix A of Petit et al. 2011). Of course, this model was chosen with a small sample of 13 detached objects. The known detached objects in our sample now number 58, but we still find that some sort of tapering beyond ~39–40 au in the intrinsic population is necessary to be consistent with current observations.

We emphasize that we are not claiming this two-component uniform q distribution is a wonderful description of the real detached objects. A more complex parametric model for q could easily be developed. We simply use this as a relatively simple nonrejectable model to produce the population estimates below, which is the main goal of this paper. The reader might wonder why $q_{split} = 40.5$ au has been selected by the tests, rather than something closer to the 38.5 au value evident in Figure 1. The reason is simply that the small tail of $q < 35$ au detached objects forces the assumed linear behavior from the minimum of 34 au to be a poor representation of the low-q portion of the distribution. If we arbitrarily cut away the small $q < 35$ au section of the real and simulated samples, the same analysis now yields a cumulative q distribution (Figure 6, top panel) with $q_{split} = 38.5$ that provides a better match to the distribution (with an A-D probability of 27%) and looks visually more like the real detections.

4.1. Population Estimate

Our method for estimating the population (the debiased number of objects) follows similar projects in the literature (e.g., Kavelaars et al. 2009; Petit et al. 2011; Gladman et al. 2012; Lawler et al. 2018b; Ashton et al. 2021; Crompvoets et al. 2022). For a given trial, we let the survey simulator run until it detects the same number of detached objects as the real sample, recording how many objects it had to draw to do so; this drawn number is the population estimate for that trial. We bin 1000 trials, take the median to be our nominal population estimate, and determine the 95% confidence interval from the 25th and 975th values in a sorted list (2.5% wings on either side of the distribution). This gives a result for a population of detached objects with $H_r < 8.66$ of

$$N(H_r < 8.66) = 36{,}000^{+12{,}000}_{-9000} \quad \text{(parametric estimate)} \quad (1)$$

in the semimajor axis range 48–250 au. This is the first observational population estimate of the detached objects based on independently determined orbit distributions and is an important goalpost for cosmogonic models.

To investigate the dependence of the population estimate on our specific perihelion parameterization, we repeat the estimate procedure for two additional cases in the two-component perihelion model (orange squares in Figure 4, whose q distributions are shown the bottom two panels of Figure 6). For $q_{split} = 39.0$ au and $f_{low} = 0.59$, which, according to Figure 4, is at the threshold of rejectability (lower left end of the acceptable region), this model gives a median population of $37{,}000^{+10{,}000}_{-9000}$, within 3% of the least-rejectable model. Similarly, at the upper right boundary, a model with $q_{split} = 42.5$ au and $f_{low} = 0.99$ produces a very similar median population of $35{,}000^{+11{,}000}_{-9000}$. This illustrates two important points. First, it tells us that the population estimate is not strongly coupled to the particular choice of q distribution (despite the match obviously appearing inferior in Figure 6). Second, it tells us that the uncertainty on our population estimate is still dominated by the Poisson error from the small number of known detached TNOs rather than the specifics of a perihelion model.

5. Survey Simulation of a Rogue Planet Model

Having determined a nonrejectable parametric description of the detached TNO orbit and size distributions, we now switch our focus to another application of the same machinery. We are able forward-bias orbital element models and produce a population estimate without any parametric distributions. Using the previously established methodology, we can compare the results of a numerical simulation to the OSSOS detached data set. As one illustrative example, we consider the results of a numerical

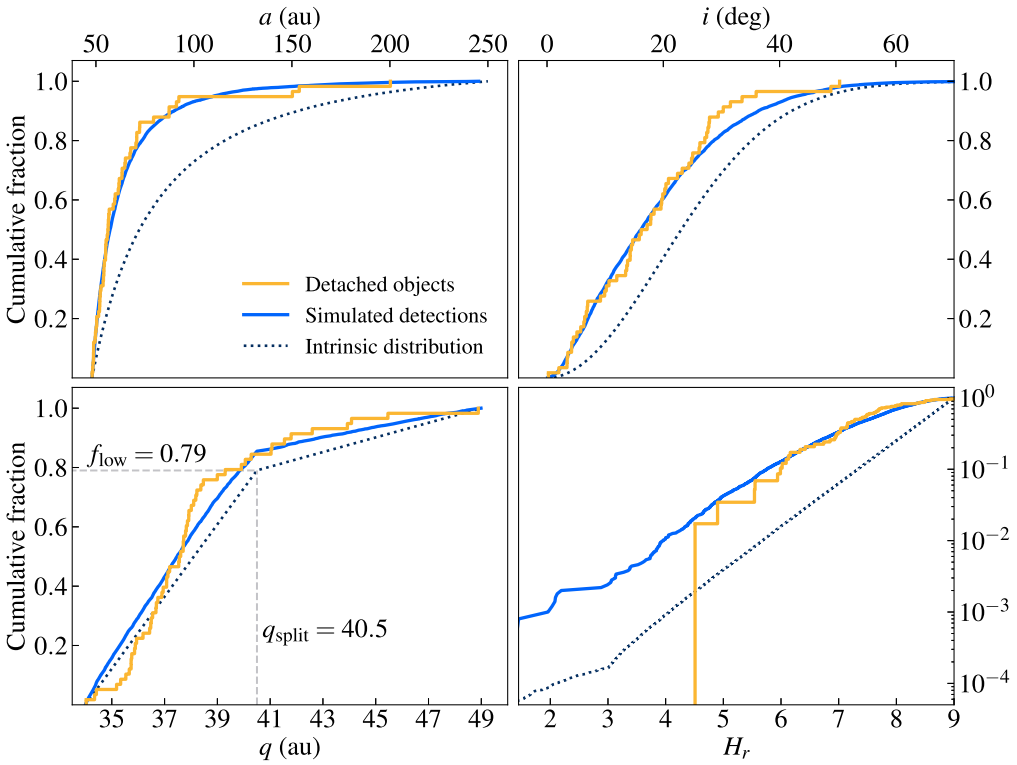

Figure 5. Cumulative distributions of the OSSOS detached objects (gold), simulated detections (blue), and the intrinsic model (dotted black) in the two-component q model with the least-rejectable combination $q_{split} = 40.5$ au and $f_{low} = 0.79$, as indicated by the light gray dashed lines in the lower left panel. The A-D probabilities for a, q, i, and H are 89%, 14%, 65%, and 26%, respectively. We use this nonrejectable model to estimate the number of detached objects in Section 4.1.

simulation (Huang et al. 2022) of a rogue planet scenario, which is a possible explanation for the perihelion lifting of the detached objects (Gladman & Chan 2006). In such a scenario, an Earth-mass or greater planet forms in the outer solar system contemporaneously with the other planets; strong giant planet interactions initially launch the rogue to a large semimajor axis followed by a period of weak perturbations while the rogue exists on a metastable orbit in the scattering disk. During this period, the rogue strongly influences the early TNOs, including the primordial scattering population. Such rogue planets are ejected via scattering on a 100 Myr timescale (Gladman & Chan 2006). We compare the output of one particular rogue planet numerical integration to the observed orbital distributions of the detached objects discovered in OSSOS.

We have access to the results of a recent rogue planet simulation (Huang et al. 2022); it is important to note that the rogue's mass and orbit have not yet been tuned in any way to "fit" the observed detached objects. The rogue is a 2 $M_\oplus$ planet that starts the perihelion-lifting simulation with $a = 300$ au, $q = 40$ au, and $i = 20°$. The Sun and giant planets start on their current orbits, mutually interacting and (weakly) affecting the rogue's orbit. There are 10^5 test particles that represent the primordial scattering TNOs, which are initially distributed from 50 to 600 au following a $dn/da \propto a^{-2.5}$ power law. The initial q_0 of the test particles are uniformly assigned from 33 to 37 au, and the initial i is distributed according to $\sin(i)$ times a Gaussian with width $\sigma_i = 15°$ (as observed in the hot main-belt classicals).

The initial conditions are then integrated forward 100 Myr using GLISSER, an improved GPU-based planetary system integrator based on Zhang & Gladman (2022) but now with the capability to resolve test-particle close encounters with the massive bodies. Over 100 Myr, the rogue's semimajor axis has a variation of no more than ±30 au. After 100 Myr, the rogue is manually removed from the system (for more details, see Huang et al. 2022). The system, sans rogue, is then integrated forward to 4 Gyr to bring the orbital distributions to the present epoch for comparison with observations; there are only mild modifications to the detached population because, after the rogue leaves, most $a < 250$ au detached TNOs are "frozen into place." The $q \lesssim 35$ scattering TNOs are especially heavily depleted as Neptune "erodes" this population, although a few can "stick" to resonances (Duncan & Levison 1997; Lykawka & Mukai 2007; Yu et al. 2018). Lastly, the surviving test particles are classified by the algorithm described in Gladman et al. (2008), which analyzes the 10 Myr behavior of each particle. We use the "detached" test particles with semimajor axes between 48 and 250 au as the "intrinsic model" from which we draw objects during the survey simulation. Figure 7 shows the 4 Gyr end-state of the simulation, as well as the 58 OSSOS TNOs and twice as many simulated detections (for illustrative purposes). Here we do not compare to objects classified as resonant because their selection effects are more complicated. Although the simulated detached TNOs of Figure 7 clearly exhibit a bias to lower a, q, and i, as seen in the real detached TNOs, there appear to be comparatively more simulated detections at large a; this is shown quantitatively in the cumulative distribution in Figure 8.

Survey simulation of this rogue planet integration was also performed by Huang et al. (2022); however, we take a more rigorous approach and focus exclusively on the OSSOS detached sample at all q.[9] Selecting all of the detached

[9] Huang et al. used all $q > 38$ au objects available from the Minor Planet Center, but for this sample, precise debiasing is not possible.

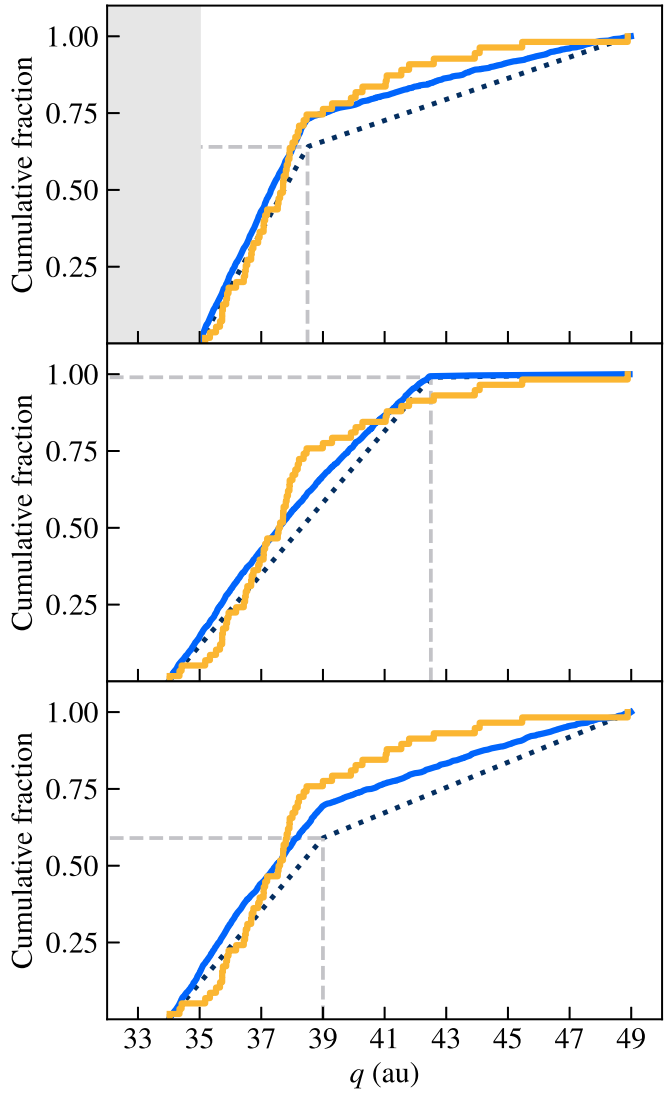

Figure 6. Top panel: nonrejectable ($P = 27\%$) simulated q distribution plotted after having arbitrarily removed the $q < 35$ au detached objects (gray region). Without the extended low-q tail seen in the q panel of Figure 5, the real detached distribution appears to be more similar to our heuristic two-component model with $q_{\rm split} = 38.5$ au; for $f_{\rm low} = 0.64$, one obtains a break in the simulated detections that is nearly identical to the one in the real detached distribution. Middle and bottom panels: two other perihelion distributions, both on the threshold of rejectability ($P \simeq 5\%$), from the two-component model. The middle and bottom panels correspond to the upper right and lower left orange squares, respectively, in Figure 4. The inferior match of these models is illustrative of the quality of fit at the limit of acceptability. (Note that the e distributions for these two cases are statistically acceptable, $P \approx 50\%$, as is the a distribution, illustrating the superior diagnostic value of using the q distribution as mentioned in Section 2.)

classifications with 48 au $< a <$ 250 au from the simulation's output, we used the survey simulator in lookup mode and applied the H distribution from Section 2.2. We generated 5000 simulated detections based on the detached object output of the rogue planet simulation. The cumulative distribution plot is shown in Figure 8. The A-D test results for a, q, i, and H are 0.01%, 40%, 76%, and 45%, respectively.

We find that the action of the rogue planet generates q and i distributions that are nonrejectable with no significant exploration of the rogue simulation's parameter space. Surprisingly, this first simulation is able to reproduce the whole detached perihelion distribution (see the q panel of Figure 8) better than any of our parametric models. Additionally, despite being initially distributed with a colder inclination width of only 15° (recall that this was rejectable at >99% confidence in Section 2.1), the rogue planet's effect provides enough heating in i to produce the large-i tail and is an excellent match, despite not being tuned to do so. The main mechanism by which q and i increase from the initial conditions is Kozai cycling within MMRs (reviewed by Gomes et al. 2008). This secular effect causes a correlated increase in q and i when an object falls into an MMR of Neptune, and if the object drops out of the resonance (either by Neptune migration or by changing a due to close encounters with the rogue), the higher q and i are "frozen" in place. Lastly, it is unsurprising that the H distribution is nonrejectable, since we are assigning H values to model objects post facto during the survey simulation.

There is, however, a significant discrepancy between the real detached semimajor axis distribution and the survey-simulated distribution (which is strongly rejected). The intrinsic distribution from the simulation contains a smaller fraction of objects at low a, which results in fewer simulated detections at low a when compared to the real detached TNOs (see Figure 8). The discrepancy at the small-a tail of the distribution is the cause of the extremely small A-D test probability (0.01%), as the A-D test is very sensitive to the tails. For comparison, the K-S test (less sensitive to the tails) for a indicates an order of magnitude less rejectability than the A-D result, suggesting that the small-a tail is indeed the issue, even though the K-S test indicates a probability of <1%. We find that the low-a discrepancy is entirely due to the region between the 2:1 and 5:2 MMRs; if we restrict to only real and simulated detections with $a > 57$ au, then the a-distribution problem disappears (with an A-D probability of 57%), and none of q, i, and H are made rejectable either. This mismatch indicates that this sample numerical simulation is missing some physics (although it is possible that some stochastic evolution in the rogue's history could increase implantation $a < 57$ au TNOs). More likely, the simulation used as an example here lacks the physics of migration, which has been shown (Nesvorný et al. 2016) to be especially effective at populating the semimajor axis range due to the abundance of MMRs.

Based on this cosmogonic simulation (in which the orbital element distributions are not fit to each orbital parameter), the usual population analysis yields an estimated detached TNO population (with $H_r < 8.66$ and 48 au $< a <$ 250 au) of $48{,}000^{+15{,}000}_{-12{,}000}$. This estimate is larger than Equation (1) because the rogue simulation possesses a set of larger-q TNOs that are extremely difficult to detect; the existence of such TNOs would require more intrinsic objects for the survey simulator to detect the 58 real TNOs. Figure 8 shows that roughly one-third of the intrinsic TNOs in this simulation have $q > 50$ au, and these are not expected to be detected even in a survey as large as OSSOS. We believe it very likely that in reality, there are $q > 50$ au TNOs in the $a < 250$ au region, as predicted by numerical simulations (Gladman & Chan 2006; Lykawka & Mukai 2008; Nesvorný et al. 2016; Huang et al. 2022), which thus forces up our population estimate.

6. Discussion and Conclusions

We first discuss the similarities of our detached population estimate to the few that exist in the literature and then compare it to populations of other dynamical classes for context.

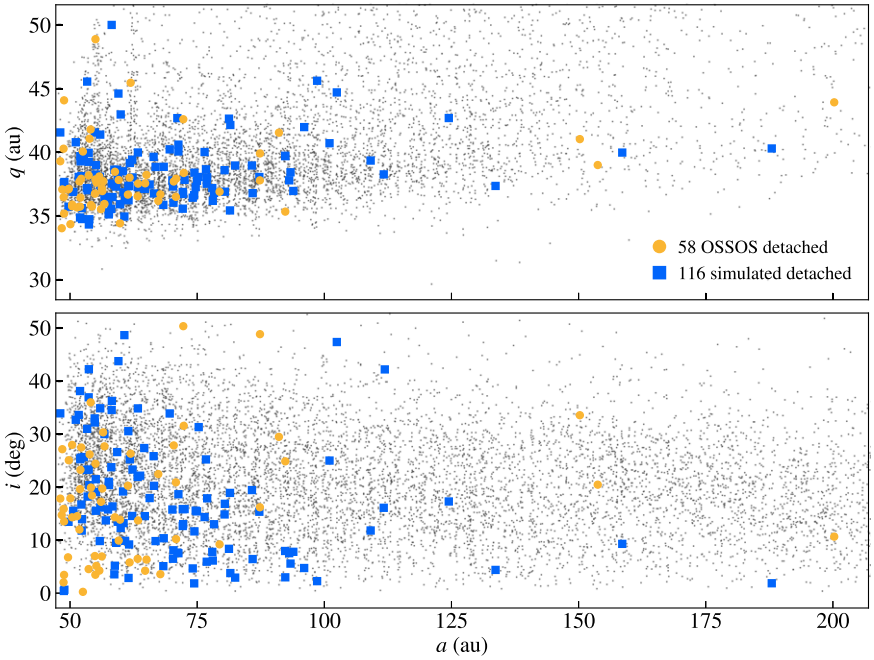

Figure 7. The 58 TNO OSSOS sample we are using, compared with the intrinsic distribution (black dots) provided by the 4 Gyr end-state of a numerical simulation with a rogue planet that inhabited the distant solar system for 100 Myr (see text). The blue squares show a set of (twice as many) simulated detections from the intrinsic distribution, illustrating the detection bias to lower a, q, and i.

6.1. Comparison to Other Detached Estimates

Our parametric detached population estimate (Equation (1)) was 36,000 TNOs, with a variation due to the model systematics that is smaller than the 30% variation coming from the Poisson statistics. The orbital distribution coming from the single rogue planet simulation we examined had a portion of the detached population with harder-to-detect orbits, but even this only increased the estimate to 48,000, again with 30% Poisson uncertainties (at 95% confidence).

Because of these variations, and because some $q > 50$ au component is extremely likely to exist, we believe our results justify only a single significant figure, and we estimate to roughly 50% accuracy:

$$N(H_r < 8.66) = (5 \pm 2) \times 10^4 \quad (48 \text{ au} < a < 250 \text{ au}). \tag{2}$$

The only systematic effect that could likely invalidate this is if there is an enormous hidden population of $q \gg 50$ au detached objects with $a < 250$ au. Observations indicate a lack of $q > 50$ au objects below some a threshold, which has been used as a constraint on the production mechanism of sednoids (Morbidelli & Levison 2004; Gladman & Chan 2006; Trujillo & Sheppard 2014). The recent Dark Energy Survey (Bernardinelli et al. 2022) found no $q > 50$ au detached objects[10] out to $a = 500$ au.

The only other direct observational estimate of the full 48 au $< a < 250$ au detached population is from the CFEPS project; Petit et al. (2011) estimated $N(H_g < 8) = 10,000^{+7000}_{-5000}$ for all nonscattering TNOs with $a > 48$ au (assuming a $dn/da \propto a^{-2.5}$ distribution, which is thus effectively an estimate for $a < 250$ au, since only 8% of the TNOs are beyond 250 au for that semimajor axis). We adjust H_g to H_r by adopting their assumed $g - r = 0.7$ color, making their 10,000 estimate correspond to $H_r < 7.3$. The CFEPS extrapolated down to a 100 km diameter ($H_r \simeq 8.66$) by using the same (steep) $\alpha = 0.8$ slope as for their relatively bright detections, but deeper surveys prefer shallower values of α (Fraser et al. 2014; Kavelaars et al. 2021). For consistency, we scale from $H_r = 7.3$ to 8.66 using our $\alpha = 0.6$ and keep 92% of the population to restrict to $a < 250$ au, resulting in the Petit et al. study suggesting 60,000 detached TNOs, with a factor of 2 error bar just from the statistics and some additional uncertainty from the unknown α. This estimate is thus consistent with our new study, which, unlike Petit et al., has been matched to the better-determined orbital distribution now that there are more known detached TNOs.

Although not based directly on observations of detached objects, Nesvorný et al. (2016) used the results of their outer solar system emplacement model caused by grainy outward Neptune migration to estimate a detached population of 40,000 $D > 100$ km TNOs with a more restricted semimajor axis range of 50 au $< a < 100$ au. Since we have concluded that the detached a distribution follows $dn/da \propto a^{-2.5}$, this trims our 50,000 48 au $< a < 250$ au distribution to 33,000 and is thus very consistent with the Nesvorný et al. estimate. Although this grainy migration model was not compared to the details of the orbital distribution of detached objects, the number match is impressive given that the absolute normalization was set by the need to capture enough Jupiter Trojans in the same process. A comparison incorporating bias needs to be done for the a, q, and i distributions of these models. However, there also appears to be an obvious problem when looking at the detached-to-resonant ratio (see below).

6.2. Comparison to Other Dynamical Classes

A proposed cosmogonic model should be able to produce both the absolute population of the detached component, as

[10] Object 2014 US_{277} is likely to be in the 6:1 resonance (P. Bernardinelli 2022, private communication).

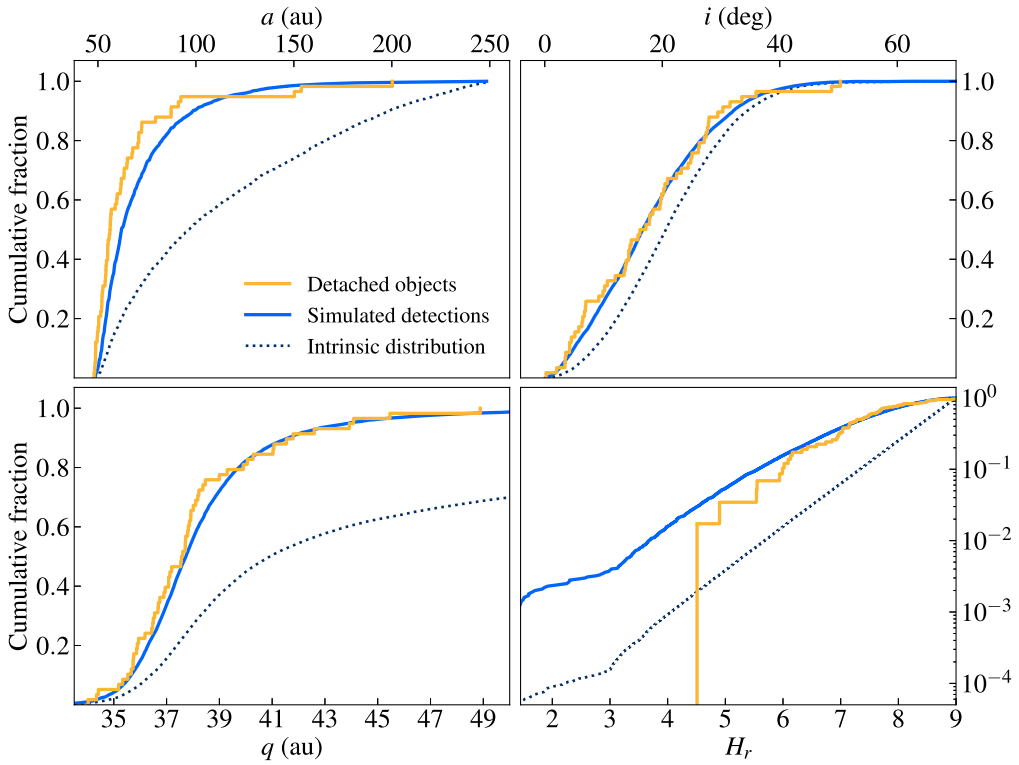

Figure 8. Intrinsic distribution and simulated detections coming from the end-state of a numerical rogue planet simulation (see text). This simulation has a larger fraction of objects at high-a and high-q orbits, but when the biased detections are compared to the real detached objects, one sees that the perihelion distribution (lower left) provides an excellent match, with an A-D probability of 40%.

well as its relative numbers compared to the hot main belt, and the resonant and scattering components in the same semimajor axis range.

Hot main Kuiper Belt.—The hot main-belt estimate from Petit et al. (2011) is $N(H_r < 7.3) = 4100^{+900}_{-800}$; scaling by a factor of $10^{0.6(8.66-7.3)}$ gives $N(H_r < 8.66) = 27{,}000^{+6000}_{-5000}$. We thus estimate that detached objects outnumber the main belt by a factor of $\simeq$2, comparable to Petit et al.'s (2011) ratio of 2.5. If the detachment of ancient scattering TNOs into the hot main belt is comparably efficient to that beyond the 2:1, one might expect that the ratio of $a > 48$ au detached to the hot main belt would just follow the ancient semimajor axis distribution. For an $a^{-2.5}$ power law, the ratio of numbers from 48 au $< a <$ 250 au to 40 au $< a <$ 48 au is 3. This is possibly interesting as a constraint on the detachment physics and continues to be in line with the "unification" model of Petit et al. (their Section 5.2.3) that supports the idea that all of the hot populations derive from a single cosmogonic process.

Today's scattering population.—Petit et al. (2011) used the CFEPS survey to estimate $\simeq$5000 $D > 100$ km scattering TNOs with a factor of at least 3 error bar. The OSSOS-based estimate for scattering TNOs (Lawler et al. 2018b) is an order of magnitude larger at 80,000 but covers the entire scattering population out to very large a. We retrieved that model and determined that 48 au $< a <$ 250 au represented $\simeq$40% of the model; thus, in this semimajor axis range, the detached TNOs outnumber the scattering by a ratio of only $5 \times 10^4/32{,}000 \simeq 1.5$. We are surprised that the ratio is this small. The rogue planet scenario suggests an intrinsic detached/scattering ratio (today, after dynamical erosion of the age of the solar system) of 10:1, which would match the ratio based on the Petit et al. scattering estimate. For comparison, Nesvorný et al. (2016) estimated that this ratio should be 4–5. Revisiting these studies is clearly appropriate now that a reliable detached population estimate exists to compare to and should be an additional constraint on the detachment process(es).

The nearby resonant populations.—An obvious dramatic disagreement seems to be contained in the realization (Gladman et al. 2012) that the distant resonant populations are huge, with many thousands of objects in each of the main distant resonances. Most recently, Crompvoets et al. (2022) used OSSOS to estimate that the distant resonances (beyond the 2:1) contain at least 100,000 objects with $H_r < 8.66$, albeit with a factor of 4 uncertainty (at 95% confidence). Thus, in the 48 au $< a <$ 250 au range, the detached/resonant ratio is $<$0.5; to our knowledge, no emplacement models to date generate enough resonant objects at large a. The rogue simulation tested here has a ratio of 2.3 (that is, fewer resonant than detached). Nesvorný et al.'s (2016) two grainy models give 8 or 11 for the ratio of 50 au $< a <$ 100 au detached to the total of the four n:1 resonances in that range; our detached estimate in that range is 33,000 TNOs, while the sum from Crompvoets et al. of the 3:1, 4:1, 5:1, and assuming 10,000 in the 6:1 resonance, is 51,000, which gives a detached/resonant ratio of $\simeq$0.65. Thus, the huge current TNO population trapped in large-a resonances is an outstanding mystery, and we are not aware of any models to create detached TNOs that simultaneously produce sufficiently large resonant populations in the same semimajor axis range.

6.3. Conclusions

The fact that the current detached population is nicely described by the $dn/da \propto a^{-2.5}$ power law generates some interesting thought experiments. The theoretical long-term steady state for a population of scattering objects that starts

with a single semimajor axis (Yabushita 1980; Duncan et al. 1987; Malyshkin & Tremaine 1999) has a projected surface density of $\Sigma(a) \propto a^{-2.5}$, corresponding to a shallower $dn/da \propto a^{-1.5}$; this is the distribution for the scattering disk after 4 Gyr of evolution in numerical simulations (Levison & Duncan 1997). Several scenarios are possible. We have confirmed numerically that ~30 Myr after Neptune begins scattering TNOs on nearby orbits beyond $a = 50$ au, the power law is still steeper than the steady state, and we find $dn/da \propto a^{-2.5}$ at this time (hereafter the power laws are all for dn/da); if q lifting occurs across the entire 48 au $< a <$ 250 au range with a semimajor axis independent efficiency, then -2.5 could be preserved. Alternately, if the steady state (-1.5) had been reached, then if the efficiency of q lifting went as $1/a$, the -2.5 index could be reached. Lastly, if the perihelion lifting occurred extremely early, when the index was even steeper than -2.5, the probability of lifting q would have to increase with a (this would likely be the case for secular perihelion oscillations as a approaches that of the rogue). All of these scenarios are likely oversimplifications because resonance trapping (Gomes et al. 2008; Nesvorný et al. 2016; Huang et al. 2022) certainly plays a role. Only careful comparisons between the final (4.5 Gyr) states of cosmogonic numerical simulations and calibrated observational surveys with bias measurements (like the preliminary comparison we did here between a rogue planet simulation and OSSOS) are likely to be convincing as observational surveys advance and numerical studies improve.

The population comparisons to other dynamical classes (Section 6.2) are made possible by now having (what we believe to be) a reliable estimate of the detached population's numbers, albeit still with 50% uncertainty at 95% confidence. Since the systematics seem to be under control (with model variations causing population variations less than the 95% confidence intervals), more characterized detections will be required to improve the estimate. The Legacy Survey of Space and Time at the Vera C. Rubin Observatory should certainly provide better statistics of detached detections.

With our number estimate for the detached objects, a (more uncertain) total mass estimate can be made (in this a range and to a limiting magnitude/size). The mass will be dominated by the large number of objects with $3 < H_r < 8.66$, which, if we adopt a 17% albedo for detached TNOs (Santos-Sanz et al. 2012), corresponds to radii of 770 and 57 km. Fewer than 0.02% of the objects have $H_r < 3$ ($D > 770$ km) for our assumed H-magnitude distribution. Writing the differential size distribution $dn/dR = kR^{-(5\alpha_*+1)}$ (see footnote in Section 2.2) with $\alpha_* = 0.6$, we obtain the normalization factor k by integrating this distribution to give our population of 5×10^4. Integrating the differential mass distribution yields $M \sim \rho_{\rm cgs} \cdot 3 \times 10^{26}\,{\rm cm}^3$, or $M \simeq 0.05\,M_\oplus$ using $\rho_{\rm cgs} = 1.0$ g cm^{-3}, with a factor of at least 3 uncertainty due to assumptions on the albedo and density. This just says that the detached population's total mass is comparable to the main belt.

We are impressed by the untuned improvement in the perihelion distribution that resulted from using the rogue planet simulation's output at the present epoch. Caution needs to be taken about the quality of the survey characterization in future studies; the details of the shape of the detected perihelion distribution of detached TNOs may be one of the strongest constraints on the detachment mechanism, and understanding the survey detection biases with high precision may be important to discriminate between models. Luckily, we are entering the era where the number ratio and detailed orbital distributions for the $a > 48$ au dynamical populations are becoming measurable with better than a factor of 2 precision. Improved observational estimates of the resonant and scattering should also be forthcoming and are arguably more impactful in the short term.

Acknowledgments

We acknowledge Canadian funding support from NSERC (grant 2018-04895). Y.H. acknowledges support from the China Scholarship Council (grant 201906210046) and the Edwin S.H. Leong International Leadership Fund.

ORCID iDs

Matthew Beaudoin https://orcid.org/0000-0001-6597-295X
Brett Gladman https://orcid.org/0000-0002-0283-2260
Yukun Huang (黄宇 坤) https://orcid.org/0000-0003-1215-4130
Michele Bannister https://orcid.org/0000-0003-3257-4490
J. J. Kavelaars https://orcid.org/0000-0001-7032-5255
Jean-Marc Petit https://orcid.org/0000-0003-0407-2266
Kathryn Volk https://orcid.org/0000-0001-8736-236X

References

Alexandersen, M., Gladman, B., Kavelaars, J. J., et al. 2016, AJ, 152, 111
Anderson, T. W., & Darling, D. A. 1954, Journal of the American Statistical Association, 49, 765
Ashton, E., Gladman, B., Kavelaars, J. J., et al. 2021, Icar, 356, 113793
Bannister, M. T., Kavelaars, J. J., Petit, J.-M., et al. 2016, AJ, 152, 70
Bannister, M. T., Shankman, C., Volk, K., et al. 2017, AJ, 153, 262
Bannister, M. T., Gladman, B. J., Kavelaars, J. J., et al. 2018, ApJS, 236, 18
Batygin, K., Adams, F. C., Brown, M. E., & Becker, J. C. 2019, PhR, 805, 1
Batygin, K., Mardling, R. A., & Nesvorný, D. 2021, ApJ, 920, 148
Bernardinelli, P. H., Bernstein, G. M., Sako, M., et al. 2022, ApJS, 258, 41
Bernstein, G. M., Trilling, D. E., Allen, R. L., et al. 2004, AJ, 128, 1364
Brasser, R., & Schwamb, M. E. 2015, MNRAS, 446, 3788
Brown, M. E. 2001, AJ, 121, 2804
Brown, M. E. 2008, in The Solar System Beyond Neptune, ed. M. A. Barucci et al. (Tucson, AZ: Univ. Arizona Press), 335
Chen, Y.-T., Gladman, B., Volk, K., et al. 2019, AJ, 158, 214
Crompvoets, B. L., Lawler, S. M., Volk, K., et al. 2022, PSJ, 3, 113
Duncan, M., Quinn, T., & Tremaine, S. 1987, AJ, 94, 1330
Duncan, M. J., & Levison, H. F. 1997, Sci, 276, 1670
Fraser, W. C., Brown, M. E., Morbidelli, A., Parker, A., & Batygin, K. 2014, ApJ, 782, 100
Gladman, B., & Chan, C. 2006, ApJ, 643, L135
Gladman, B., Holman, M., Grav, T., et al. 2002, Icar, 157, 269
Gladman, B., Marsden, B. G., & Vanlaerhoven, C. 2008, in The Solar System Beyond Neptune (Tucson, AZ: Univ. Arizona Press), 43
Gladman, B., & Volk, K. 2021, ARA&A, 59, 203
Gladman, B., Lawler, S. M., Petit, J.-M., et al. 2012, AJ, 144, 23
Gomes, R. S., Fernández, J. A., Gallardo, T., & Brunini, A. 2008, The Solar System Beyond Neptune (Tucson, AZ: Univ. Arizona Press), 259
Gomes, R. S., Matese, J. J., & Lissauer, J. J. 2006, Icar, 184, 589
Gulbis, A. A. S., Elliot, J. L., Adams, E. R., et al. 2010, AJ, 140, 350
Huang, Y., Gladman, B., Beaudoin, M., & Zhang, K. 2022, ApJL, 938, L23
Kaib, N. A., & Sheppard, S. S. 2016, AJ, 152, 133
Kavelaars, J. J., Petit, J.-M., Gladman, B., et al. 2021, ApJL, 920, L28
Kavelaars, J. J., Jones, R. L., Gladman, B. J., et al. 2009, AJ, 137, 4917
Khain, T., Becker, J. C., Lin, H. W., et al. 2020, AJ, 159, 133
Lawler, S. M., Kavelaars, J. J., Alexandersen, M., et al. 2018a, FrASS, 5, 14
Lawler, S. M., Shankman, C., Kaib, N., et al. 2017, AJ, 153, 33
Lawler, S. M., Shankman, C., Kavelaars, J. J., et al. 2018b, AJ, 155, 197
Levison, H. F., & Duncan, M. J. 1997, Icar, 127, 13
Lykawka, P. S., & Mukai, T. 2007, Icar, 192, 238
Lykawka, P. S., & Mukai, T. 2008, AJ, 135, 1161

Malhotra, R. 2019, GSL, 6, 12
Malyshkin, L., & Tremaine, S. 1999, Icar, 141, 341
Morbidelli, A., & Levison, H. F. 2004, AJ, 128, 2564
Morbidelli, A., Levison, H. F., & Gomes, R. 2008, The Solar System Beyond Neptune (Tucson, AZ: Univ. Arizona Press), 275
Nesvorný, D. 2018, ARA&A, 56, 137
Nesvorný, D., Vokrouhlický, D., & Roig, F. 2016, ApJL, 827, L35
PetitJ. M., KavelaarsJ. J., GladmanB., & AlexandersenM. (2018) OSS: OSSOS Survey Simulator, Astrophysics Source Code Library, ascl:1805.014
Petit, J.-M., Kavelaars, J. J., Gladman, B. J., et al. 2011, AJ, 142, 131
Petit, J.-M., Kavelaars, J. J., Gladman, B. J., et al. 2017, AJ, 153, 236
Pike, R. E., & Lawler, S. M. 2017, AJ, 154, 171
Santos-Sanz, P., Lellouch, E., Fornasier, S., et al. 2012, A&A, 541, A92
Shankman, C., Gladman, B. J., Kaib, N., Kavelaars, J. J., & Petit, J. M. 2013, ApJL, 764, L2
Shankman, C., Kavelaars, J. J., Gladman, B. J., et al. 2016, AJ, 151, 31
Sheppard, S. S., Trujillo, C. A., Tholen, D. J., & Kaib, N. 2019, AJ, 157, 139
Silsbee, K., & Tremaine, S. 2018, AJ, 155, 75
Trujillo, C. A., & Sheppard, S. S. 2014, Natur, 507, 471
Yabushita, S. 1980, A&A, 85, 77
Yu, T. Y. M., Murray-Clay, R., & Volk, K. 2018, AJ, 156, 33
Zhang, K., & Gladman, B. J. 2022, NewA, 90, 101659